Master of Advanced Studies ETH in Medical Physics

Quality guided wide field x-ray tomographic imaging

Author:
David Haberthür
University of Bern

Supervisors:
Dr. Christoph Hintermüller
Paul Scherrer Institute, Villigen
Prof. Dr. Marco Stampanoni
Paul Scherrer Institute, Villigen
ETH Zurich

April–August 2008, on and off

to whom it may concern

Zusammenfassung

Röntgentomographische Mikroskopiestationen auf dem neuesten Stand der Technik können innerhalb einiger Minuten volumetrische Daten in einer Auflösung von wenigen Mikrometern aufnehmen. Es können somit grössere Objekte aufgenommen werden, indem mehrere Tomogramme gestapelt werden und eine lokale tomographische Rekonstruktion gemacht wird.

Wenn mehrere Tomogramme gestapelt werden, erhöht dies das Sichtfeld in vertikaler Richtung. Das Ziel der vorliegenden Arbeit war es, an der TOMCAT-Strahllinie der Swiss Light Source verschiedene Aufnahmeprotokolle zu implementieren, die es ermöglichen, ein grösseres Sichtfeld in horizontaler Richtung zu erreichen. Dafür wurden verschiedene Messprotokolle an der Strahllinie implemetiert. Wir konnten zeigen, dass das laterale Sichtfeld von TOMCAT vergrössert werden kann und es möglich ist, tomographische Aufnahmen von Objekten in der vom Endbenutzer gewünschten Qualität in einer automatischen und unbeaufsichtigten Art und Weise aufzunehmen.

Abstract

State-of-the-art synchrotron-based tomographic microscopy end-stations acquire volumetric data at micrometer level within a few minutes. It is therefore possible to investigate large objects at a high resolution by stacking several tomograms together and perform a local tomographic reconstruction.

The stacking of tomograms increases the field of view in vertical direction. The present work aims to implement the necessary acquisition protocols at the TOMCAT beamline of the Swiss Light Source to increase the field of view of the tomographic imaging process in horizontal direction. It is the base for imaging of samples bigger than the size currently possible. Different image acquisition protocols have been implemented for the end-user at the beamline. We have shown that we can increase the lateral field of view of TOMCAT and provide the end-user of the beamline the possibility to acquire quality guided tomographic wide field scans of his sample in an unattended, automatic way.

Acknowledgments

I thank PD Dr. Johannes C. Schittny for the generosity of letting me follow the Master of Advanced Studies Course in Medical Physics parallel to my Ph.D. studies. It has been a demanding and very fascinating opportunity for me.

Dr. Christoph Hintermüller was a great help while supervising this present work, I thank him for expert help with all things C++, MATLAB, Tomography, for valuable discussion in the office and also for the not so valuable ones during lunch breaks.

Prof. Dr. Marco Stampanoni was very generous in making it possible that the present work has been performed at the Paul Scherrer Institute. His deep insight in tomographic imaging and the guidance on this project have been of tremendous value.

Dr. Federica Marone, Dr. Samuel McDonald and all the other members of the TOMCAT group helped me to feel welcome at the PSI and made it possible that this thesis turned out to be both challenging and very interesting. Thanks for all the fruitful discussions – not only about science – we shared.

Without my family I would not be where I am today. Mom, Dad and Nina, I'll always be grateful to all of you.

Nina[1]Hostettlers good thoughts, her presence even when not at my side, her smile and love make me happy. I hope you like the bike. I love you!

[1]Note that both my sister and girlfriend share the same first name, but they are different persons.

Contents

1. Introduction **3**
1.1. Background . . . 3
1.2. Aim . . . 4
1.3. The Swiss Light Source . . . 5
1.4. TOMCAT . . . 5

2. Theory of computed tomography **11**

3. Preliminary simulations **15**
3.1. Reflections on quality . . . 15
3.2. Preliminary simulation . . . 15
3.3. Protocol definition . . . 18
3.4. Stitching really big samples . . . 19

4. Simulation of the protocols **21**
4.1. Results . . . 22
4.2. Discussion . . . 22

5. Experimental proof **25**
5.1. Materials and methods . . . 25
5.2. Post-processing and reconstruction . . . 26
5.3. Results . . . 26
5.4. Discussion . . . 26
5.5. Overlapping scans . . . 29
5.6. Integration of the wide field scan at the beamline . . . 30

6. Concluding remarks and outlook **33**
6.1. 360° versus 180° scans 34
6.2. Partial reconstructions of the scanned samples 34

Bibliography **35**

A. Scripts used in this master thesis **39**
A.1. MATLAB- simulation.m and accompanying functions 39
A.2. MATLAB - do_simulate.m 39
A.3. MATLAB - do_CompareReconstructions.m 39
A.4. MATLAB - do_correlationFFT.m 40
A.5. MATLAB - widefieldscan.m and accompanying function 40
A.6. Python - widefieldscan.py 40

List of Figures

1.1. Schematic TOMCAT beamline setup 6
1.2. TOMCAT end-station overview and detail 7

2.1. Originals and Sinograms 13

3.1. Error plot of preliminary simulations 17

4.1. Quadratic error between reconstructions and gold standard 23

5.1. Concatenated Images for the different protocols 27
5.2. Averaged quadratic error between reconstructions and gold standard . . . 28
5.3. Images resulting from a wide field scan with five overlapping sub-scans . . 31
5.4. Quality versus time 32

List of Tables

1.1. Detailed properties of the first optical system 8
1.2. Detailed properties of the second optical system 8

3.1. Details of the defined scanning Protocols 19

CHAPTER 1

Introduction

1.1. Background

Synchrotron radiation based x-ray tomographic microscopy (SRXTM) is a powerful method for the non-destructive three-dimensional imaging of a broad kind of materials with a resolution on the micrometer scale.

At TOMCAT – the beamline for TOmographic Microscopy and Coherent rAdiology experimenTs [1] at the Swiss Light Source at the Paul Scherrer Institute in Villigen, Switzerland – more than 20 user groups are presently working in very different research areas, ranging from biology, medicine and palaeontology to materials science, geology and process engineering. SRXTM enables the user to have a qualitative and quantitative measurement and analysis of nearly any structure.

In material science, SRXTM has been used for to observe inter-granular corrosions in aluminum aerospace alloys [2], to gather information from geologic samples in order to simulate fluid migration and dissolution [3], to detect cracks in hardened cement [4], to investigate impurities in ice [5], to visualize microstructures in wood [6] and for the direct investigation of processing steps [7].

In the biological field, SRXTM has been used as a tool for studying age dependent vascular alterations in genetically modified mice [8, 9], to study radiation damage to the vascular structure in the mouse brain [10] and to investigate the effect of tenascin C deficiency in the alveolarization process during the postnatal lung development [11]. SRXTM has helped to asses failure of whole bones [12], has enabled the visualization of bone vasculature in genetically distinct mouse strains [13], made the non-destructive

studying of palaeontological samples possible [14–17] and helped to obtain data for finite element modeling of the pulmonary acinus [18].

1.2. Aim

1.2.1. Development of a wide field scan protocol

Various applications depend on the availability of high resolution tomographic images of the studied sample. The available field of view (FOV) of microscopy based imaging methods like synchrotron based tomographic beamlines and micro-computed tomography stations is limited through the camera and microscope optics. A bigger FOV implicates a coarser resolution so that at resolutions of 1 µm the diameter of the sample has to be smaller than 1 mm or the sample has to be scanned locally, which is both not always possible and desired.

The vertical direction of the FOV can easily be enlarged by stacking multiple scans on top of each other. At TOMCAT, this has been implemented for end-user application; the whole end-station setup is controlled in such a way that the sample position in vertical direction is controlled with very high accuracy. This means that the final reconstructions can simply be stacked on top of each other, even if they have been acquired in different scans and the scanning time linearly increases with the sample size.

For horizontally enlarging the FOV, it is necessary to stitch together several projection images which have been obtained laterally over the full sample width prior to reconstructing the sample. This leads to a linear increase in imaging and post-processing time as compared to a standard scan.

The main goal of this thesis was to implement a so-called wide field scan at TOMCAT including the definition of scanning protocols for the achievement of a bigger FOV while keeping the total scan time as short as possible. We implemented different protocols with defined differences in reconstruction quality where the user can choose from. These protocols vary from a very fast wide field scan which introduces some reconstruction artifacts to a time-saving scan which features no decrease in quality compared to a gold standard scan. The wide field scan had to be implemented in such a way that the possibility to afterwards extract a region of interest (ROI) from the sample in high resolution was maintained.

1.2.2. Implementation at the beamline

Since the end-user of the beamline wants to have a simple mean of selecting a protocol that suits his needs of balancing between reconstruction quality and total scanning time, we have to provide a method for him to choose such a protocol. We developed a simple script with MATLAB™ (7.3.0.298 (R2006b), The MathWorks, USA) which asks the user to input relevant scanning parameters and outputs a plot of the different resulting

reconstruction qualities compared to the expected scanning time (see section 5.6). After the user chooses a protocol that suits his needs, a script is started, which sets the according scan parameters of the beamline and performs the scan unattended.

1.3. The Swiss Light Source

The Swiss Light Source (SLS) is a third generation synchrotron which is located in the western part of the Paul Scherrer Institute (PSI) in a building shaped like a giant donut with an outer diameter of 138 m, an inner diameter of 32 m and a height of 14 m. A powerful air conditioning system and effective insulation keeps the temperature inside the building within ± 0.5 °C of 23 °C during winter and 25 °C during summer. Inside the accelerator tunnel air jets maintain an average temperature of 24 °C with a tolerance of only ± 0.05 °C [19]. All the outside facing windows are strongly slanted to avoid heating of the inside of the building by direct sunlight, while still allowing a legitimate swiss work area.

1.4. TOMCAT

The beamline TOMCAT is one of thirteen operating beamlines at the SLS. It is located at the port X02DA of the SLS. The beamline receives photons from a 2.9 T super-bending magnet. Figure 1.1 shows a schematic layout of the beamline. The critical energy of this super-bending magnet is 11.1 keV (corresponding to a wavelength of 0.122 nm). Detailed technical specifications of the beamline and beam characteristics have been described by Stampanoni et al. [1], Stampanoni et al. [20].

At TOMCAT the user can perform absorption as well as phase contrast imaging with an isotropic voxel size ranging from 0.360 µm up to 14.8 µm depending on the chosen magnification.Typical acquisition times are in the order of few minutes for a full sample, depending on the selected energy and resolution.

1.4.1. End-station

The tomographic microscopy end-station is equipped with a sample holder on top of a rotation or centering stage which can be positioned with a sample stage. The integrated rotation stage allows the user to fine-tune the centering of the sample with respect to the beam. An overview of the end-station setup is shown in figure 1.2.

Sample manipulator

The sample manipulator has been designed and manufactured at the PSI and features high precision positioning possibilities of the sample to be imaged. The reproducibility of translation along the three main axis (X, Y, Z) is better than 1 µm, the centering

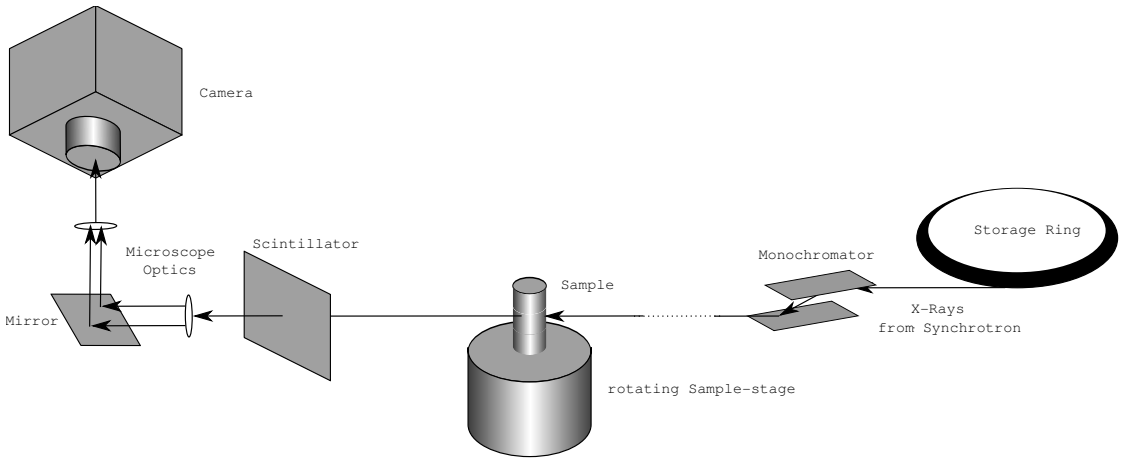

Figure 1.1.: Schematic TOMCAT beamline setup. The ring at the right depicts the storage ring of the SLS. The photons are extracted from the storage ring using a superbending magnet (not shown). The beam size is then tailored through aperture slits (not shown) and a monochromator is used to select the energy of the beam. The beam hits the sample on a rotation stage. After being attenuated by the sample the photons are converted into visible light using a scintillator. The resulting image on the scintillator is magnified using microscope optics and the resulting radiography is recorded using a CCD-camera.

motors (so-called XX- and ZZ-direction) have a reproducibility better than 0.1 µm. The rotation axis is controlled by a high-precision air bearing. The rotation speed of the sample axis can be set as fast as four revolutions per second.

The whole system can be swapped by 90°, allowing to scan thick and short samples with vertical rotation axis or long and thin samples with horizontal rotation axis. This is for practical reasons, but does not provide the users with a mean of scanning big samples with a high resolution without performing a local scan. A local scan is performed in such a way that the sample is bigger than the FOV and only the region of interest which is scanned is inside the camera window, which introduces reconstruction artifacts through so-called partial volume effects.

Microscope optics

There are currently two optical systems available at the beamline covering a field of view ranging from $0.75 \times 0.75\,\mathrm{mm}^2$ up to nearly $30 \times 30\,\mathrm{mm}^2$. The first system is based on diffraction limited microscope optics. The second system is based on a high-aperture tandem 1 to 1 configuration which is used to match the focal points of the optics and the camera. The details of both configurations are described in table 1.1 and 1.2, respectively.

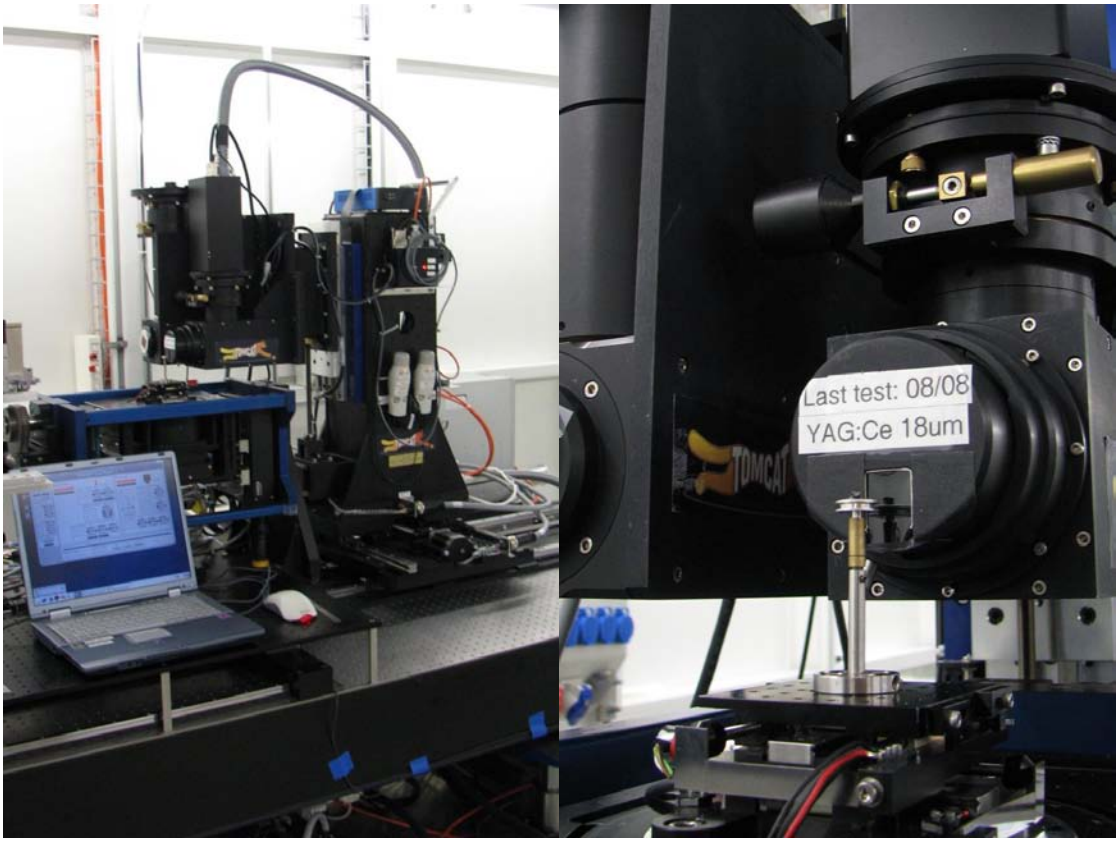

(a) Overview over the end-station: The sample stage (blue rectangular structure) with sample holder on the rotation stage can be seen in the left part of the picture. The microscope optics and CCD-camera at the end of the grey cable can be seen in the middle of the image. The laptop in front of the sample stage is used to move and rotate the sample while preparing image acquisition

(b) Detail of the microscope optics: The sample holder with a diameter of approximately 3 mm is visible in the foreground. Mounted on top of it is a standard electron microscopy sample table carrying a small piece of a rat lung. The round structure behind the sample contains the different objectives. The square visible under the label on the objective revolver is the scintillator which is used to convert the x-ray beam into visible light, which can then be recorded with the CCD-camera. See section 1.4 for details on the end-station, including the scintillator.

Figure 1.2.: TOMCAT end-station overview and detail

Table 1.1.: Detailed properties of the first optical system

Objective	Magnification	NA[a]	FOV [mm^2]	Pixel Size [µm^2]
PLAPO1.25X[b]	1.25	0.06	11.4×11.4	5.6×5.6
PLAPO2X	2	0.08	7.15×7.15	3.50×3.50
UPLAPO4X	4	0.16	3.58×3.58	1.75×1.75
UPLAPO10X	10	0.40	1.43×1.43	0.70×0.70
UPLAPO20X	20	0.70	0.72×0.72	0.35×0.35
UPLAPO40X	40	0.85	0.36×0.36	0.18×0.18

[a]Numerical Aperture
[b]PLAPO and UPLAPO are general use Plan Apochromat and Universal Plan Apochromat Olympus Objectives

Table 1.2.: Detailed properties of the second optical system

Lens	Magnification	FL[a] [mm]	FOV [mm^2]	Pixel Size [µm^2]
KinoOptik	1	150	15.1×15.1	7.4×7.4
KinoOptik	1	150	28.6×28.6	14×14

[a]Focal Length

Scintillator and camera

A scintillator[1] is used for the detection of the incident x-ray photons. It is made from a material which is excited when either charged particles or γ-quants pass through it. This excitation energy is then emitted by fluorescence photons at a longer wavelength in the form of either UV or visible light [21], which enables the detection of incident particles with a CCD-camera. At TOMCAT either a YAG:Ce or a LAG:Eu screen with varying thickness from 5 to 50 µm is available depending on the need for high spatial contrast or fast acquisition times. Both optical systems are read out by a CCD-camera featuring 2048×2048 pixels, 7.4×7.4 µm pixel size and 14 bit nominal dynamic range.

1.4.2. Post-processing and reconstruction

The transmission images are post-processed and a subset of reconstructed slices of the sample is prepared for the user. The user can preview single slices using a web-based interface, modify the desired gray value range of the reconstructions and apply different

[1]Scintillare is the latin word for twinkle or flicker.

filters and reconstruction algorithms (e.g. filtered back-projection or gridrec[2]). Once the user has checked the parameters for some slices, the reconstruction of the full sample can be initiated by submitting the data and parameters to the reconstruction cluster. The reconstructions are then computed on a 5-node Linux cluster where each node features 2 dual core processors clocked at 3.0 GHz using highly optimized reconstruction algorithms. The cluster writes the slices as stacked TIFF images (8 bit or 16 bit), in raw binary format (16 bit float) or in the native format of SCANCO scanners (.ISQ-files) depending on the preferences set by the user.

[2]at TOMCAT, a fast, FFT-based gridrec algorithm [22] is also available for the users to reconstruct their images. This algorithm is very fast, but the decrease in time comes with an increase in small artifacts in the reconstructed images. For our simulations we only used the standard filtered backprojection algorithm, since we wanted to simulate the maximal available quality that can be achieved with the different protocols.

CHAPTER 2

Theory of computed tomography

In general, computed tomography (CT) refers to the cross-sectional imaging of a sample from transmission images or projections recorded at several angular positions around the sample [23].

In medical CT-scanners, the transmission images are generally obtained while the radiation source and the detector rotate around the body part to be imaged. In micro-computed and synchrotron based tomography, the source and detector are fixed, while the sample to be imaged rotates around a chosen axis. During the imaging process multiple transmission images – essentially single radiographic images – are obtained at several angles over a 180° or 360° rotation. Before and after the scan, so-called dark and flat images (FI) are recorded. The dark images record the camera noise and dark current, while the flat images record the beam profile. After baseline correction of the projections (PI) the average of the dark images is subtracted. The projections are then normalized to the flat images as seen in equation 2.1, resulting in so-called corrected projections (CPR).

$$CPR = -ln\left(\frac{PI}{FI}\right) = ln(FI) - ln(PI) \tag{2.1}$$

The corrected projections are then transformed into so-called sinograms, where the n^{th} sinogram is composed of the n^{th} line of each projection.

The sinograms inherit their name because the Radon transformation[1] of a Dirac delta peak resembles a sine wave. The Radon transformation of a cluster of objects appears

[1] The Radon transformation was described in 1917 by Johann Radon [24] and is the mathematical basis for tomographic imaging.

as an overlay of blurred sine waves with different amplitudes and phases. Figure 2.1 (b) shows the sinograms for a simple object, (d) shows a sinogram for the so-called Shepp-Logan phantom [25] and (e) shows the sinogram for a self-drawn phantom. These phantoms have been used for preliminary tests (see section 3.2) and the simulation of the different protocols (see section 3.3).

One sinogram contains the information of one plane or slice of the reconstructed tomographic image. We can thus reconstruct the n^{th} slice of the tomographic data-set from the n^{th} sinogram using different reconstructing algorithms, e.g. a standard filtered back-projection algorithm. In a reconstructed slice, the absorption properties of the sample at a certain height are encoded by the gray values of the image.

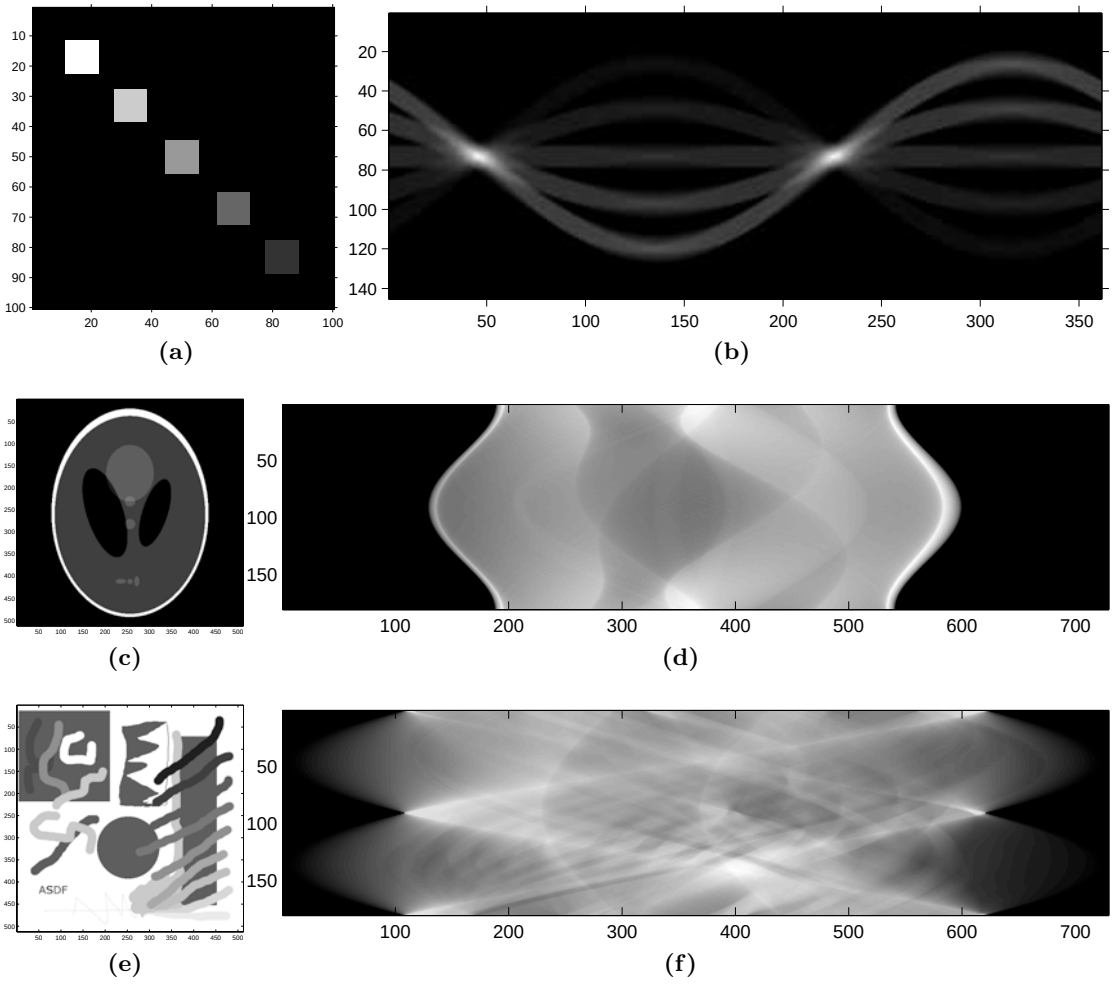

Figure 2.1.: (a): Simple object with a size of 100×100 pixels showing five squares with a side-length of 12 pixels and varying grayscale. (b): Sinogram of (a). (c): Shepp-Logan phantom with a size of 512×512 pixels showing differently sized ellipses with varying grayscales. (d): Sinogram of (c). (e): Phantom drawn by the author with a size of 512×512 pixels including different objects with varying grayscales. (f): Sinogram of (e).

CHAPTER 3

Preliminary simulations

3.1. Reflections on quality

An important question to ask in tomographic image acquisition is, how precise do we need to sample the data present in the object to obtain enough information to reconstruct it in a correct and accurate way?

In tomographic imaging we need to obtain roughly n projections over a 180° rotation of the sample to be able to accurately reconstruct an image with the dimensions of $n \times n$ pixels [23, chap. 5]. A slight violation of this demand is manageable in terms of arising artifacts. As a standard protocol at TOMCAT, 1501 projections are recorded to obtain images with a resolution of 2048×2048 pixels.

This precondition has to be considered when thinking about protocols for the imaging of bigger FOVs with a high resolution, since we have to obtain more projections at a non-central position of the sample to still obtain enough information to accurately reconstruct this part of the sample.

3.2. Preliminary simulation

MATLAB offers the function `radon` for calculating the sinogram of a two-dimensional object and `iradon` to compute the inverse Radon transformation of the sinogram or reconstruction of the slice. MATLAB was used for the simulation of different scanning protocols we want to provide to the user and for the interaction with the already present routines at the beamline. `prj2sin`, a highly optimized C++-routine [26] was used for the

generation of sinograms from the projection images and `sin2rec`, a mix of Fortran and C++-routines based on the well established filtered back-projection approach was used for the reconstruction of 2D slices.

We used the function `radon` to generate sinograms from the Shepp-Logan- and a self-drawn phantom. Different protocols were simulated by vertically interpolating parts of the original sinogram to match the defined scanning protocols, which are explained in section 3.3.

We have seen above that for an accurate reconstruction of a slice with the size of $n \times n$ pixels we need to record n projections. To see how far this constraint can be violated without introducing visible artifacts, we simulated tomographic imaging with a varying amount of projections, corresponding to so-called quality steps. Since the rows in a sinogram correspond to the number of recorded projections, we reconstructed sinograms with varying interpolated heights, corresponding to the chosen quality steps.

Based on the original, full-scale sinogram of the phantom image, we extracted lines of the sinogram with a different step width, corresponding to fewer projections obtained while imaging the sample. These sinograms were then reconstructed with `iradon` and the resulting images have been compared to the original image and the image reconstructed from n projections. To compare the different protocols, we calculated the quadratic error between the images. The results of this preliminary simulation is depicted in Figure 3.1.

The MATLAB script used for this simulation can be found in appendix A.1. Algorithm 1 lists the core details of the script in pseudo code.

Input: Phantom image
load phantom;
compute full-scale sinogram1;
for *quality = low:high* **do**
  set $N \sim \frac{1}{quality}$;
  extract every N^{th} line of sinogram1;
  interpolate this sinogram up to the full size of sinogram1;
  save as sinogram$N$;
  reconstruct sinogram$N$ to reconstruction$N$;
  calculate difference$N$ between phantom image and reconstruction$N$;
end
Output: Plot the different qualitiy steps(difference$N$);

Algorithm 1: Pseudo code representation of the MATLAB script used to generate the plot in figure 3.1.

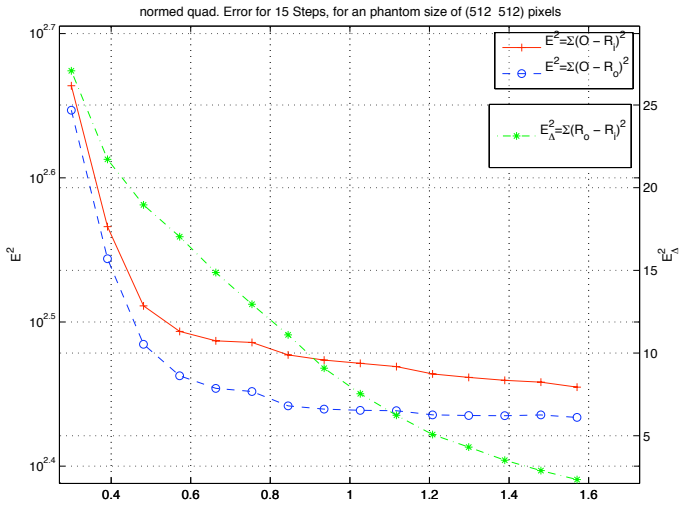

Figure 3.1.: Semi-logarithmic error plot of preliminary simulations. The red (+) plot shows the quadratic error between the Original (Shepp-Logan-Phantom) image and the reconstruction of the interpolated sinogram, the blue plot (o) shows the error between the original and the reconstruction of the full-scale sinogram. The green plot (∗) shows the difference in the quadratic errors between the first two plots (corresponding logarithmic scale on the right).

3.2.1. Results of preliminary simulation

Figure 3.1 shows the plots for 15 different quality-steps from 0.3 through $\frac{\pi}{2}$, corresponding to very few projections through n projections for a sample of size n.

As expected, the quadratic error between the phantom and the reconstruction rises quickly for low qualities. This is the case for both the interpolated and the original sinograms. The difference of the error between the original image and interpolated reconstruction to the error between the original image and the reconstruction of the image without interpolation (green line) on the other hand quickly drops for higher qualities (note the logarithmic scale).

The quadratic errors quickly (both the red and blue line) drop to a nearly horizontal line (note the logarithmic scale) after reaching a quality-step of approximately 0.6 which corresponds to an amount of $0.6 \times n$ projections for a sample of the size n. We thus defined the value corresponding to 60 % of the size of the sample to be the minimal amount of projections to record for every scanning protocol we subsequently defined.

3.3. Protocol definition

We want to implement scanning protocols for a bigger field of view in lateral direction. This can either be done in a simple way so that the transmission images are obtained at different positions laterally in the sample. These projections are then laterally stitched together prior to the reconstruction. An exemplary protocol would be to record one set of projections at the center and two 180° scans at ± one width of the FOV from the center of the sample. This would lead to three scans covering a sample approximately three times the size of one FOV. The only constraints to this is a very precise positioning of the sample compared to the camera. The disadvantage of this method is a rapid increase in projections to obtain when the sample increases in size. This is also the case if we take advantage of the 360°-imaging possibilities of TOMCAT. There we only need to move the sample from the center to one FOV-length to the side while performing a full rotation of the sample and obtain double the amount of projections. If we scale this process to bigger samples, we quickly have to record more than 10000 projections at the lateral positions to fulfill the sampling theorem for bigger samples.

Since we know that we can decrease the amount of projections and still satisfy the sampling theorem, we can obtain less projections in the center of the sample than in the outer part of the sample (the so-called ring) and still obtain enough projection images for a correct reconstruction. We thus wanted to experimentally prove the predictions obtained from the simulation and see what differences between the protocols arise. We designed the different scanning protocols in such a manner that we not only fulfil the sampling theorem, but also offer the end-user a significant reduction in scanning time compared to the gold standard.

3.3.1. Protocols used for experiments

We have seen above that we can obtain less images in the center than in the ring while still satisfying the sampling theorem and obtaining enough projections to fully reconstruct the sample. We thus defined the 6 scanning protocols described in Table 3.1. Scanning Protocol A is the so-called gold standard, where we obtain a maximal amount of projections on the left and right side of the sample and likewise in the center of the sample. Protocol B corresponds to Protocol A, but is a so-called 360°-scan, where we obtain one scan in the center of the sample and then move the sample one length of the FOV to the right and scan one full rotation of the sample. Thus we essentially record the same projections as in protocol A, but have to move the sample around less. Protocols C–F are protocols where we obtain a non-ideal amount of projections while still only slightly breaching the sampling theorem constraints, but achieving a reduction in time up to one third of the gold standard. Since the time used to obtain one full tomographic scan essentially linearly scales in time, we have simply used the amount of total projections for the calculation of the time-saving parameter.

Table 3.1.: Details of the defined scanning Protocols

Protocol	A	B	C	D	E	F
Center Projections	n/a[a]	3001	1501	1501	1001	1001
Ring Projections	n/a	6001	6001	3001	4001	2001
Total Projections	9003	9002	7502	4502	5002	3002
Time-steps used	100 %	99.98 %	83.33 %	50.01 %	55.56 %	33.34 %

[a]The Number of Projections for the Center and Ring are not available for Protocol A since we obtained three overlapping scans, each with 3001 projections to achieve a gold standard scan.

3.4. Stitching really big samples

Theoretically the amount of rings to scan consecutively is only limited by the lateral movement of the sample stage. To prove the simulation done in the next chapter, we scanned samples with one center- and one ring-scan. The whole process can be iterated to more rings, corresponding to a bigger FOV. As a proof of concept, we also scanned a sample with five overlapping scans, corresponding to one central and 2 ring scans with increasing diameter. One thing to keep in mind though is the increase in projections from ring i to $i+1$. Since the projections have to be merged together to form one big projection prior to reconstructing the slices, it is advisable to use a factor of two for the increase in projections (like we have used with the defined protocols). Since we need to interpolate the missing projections of the inner ring (or center) prior to merging to a wide field projection a factor of two facilitates the interpolation of the missing projections. If choosing another factor, e.g. a triplication from step i to $i+1$, the interpolation gets more complicated since we need to take one third of image n and two thirds of image $n+1$ to interpolate the image of position i with the image of position $i+1$.

CHAPTER 4

Simulation of the protocols

We have seen in section 3.3 that the wide field scan protocols work in such a way, that we acquire a set of images for the center of the sample over 180° and a set of images for a ring around the center over 360°. Afterwards, these images are concatenated into one big transmission image and the reconstruction is performed with this merged image. Since we obtain a different amount of images in the center compared to the amount of projections in the ring, we need to correctly interpolate the images prior to stitching. To simulate this, we implemented an interpolation of the central part of the sinograms. E.g. if we only take every second line of the central part of the sinogram and interpolate this part to the size of the outer part of the sinogram this corresponds to an amount of projections that is doubled from the center to the ring. Since we record 360°scans at the outer positions, this example actually corresponds to protocol C, as defined in table 3.1.

We implemented this approach for the simulation of all the defined protocols in a MATLAB-file, which can be found in appendix A.2. In addition to those protocols, we calculated a protocol C_1, in which we would record 6001 projections in the ring as in protocol C, but would only record 1001 projections in the central scan of the sample. We wanted to evaluate the influence of the center scan on the total quadratic error between the protocols. Protocol C_1 would reduce the needed time to 77.77 % of the gold-standard scan, but was not scanned at the beamline for confirmation of the experiments, hence it is only discussed here, but not shown in chapter 5.

Input: Phantom image
for *each protocol* **do**
  compute sinogram;
  interpolate center of sinogram according to coefficient of number of projections of the ring compared to the center;
  reconstruct interpolated sinogram;
  compute pixelwise quadratic error (E_S) to gold standard;
  compute pixelwise quadratic error (E_R) to reconstruction of the gold standard;
end
Output: plot E_S and E_R for each protocol;

Algorithm 2: Pseudo code representation of MATLAB script used to generate the plot in figure 4.1.

4.1. Results

The quadratic error between the difference image of the reconstruction of the different protocols and the gold standard is shown in fig. 4.1. This plot has been used as a mean for the comparison of the simulation with the experimental proof, which is described in chapter 5.

4.2. Discussion

We were not able to see any difference between protocol A and B, as expected, since both protocols are essentially the same. We expect a linear increase in the error for the protocols C–F, which would be in accordance to the decreasing amount of projections we record for those protocols.

If we compare the quadratic error of the reconstruction of the different protocols towards the reconstruction of the gold standard protocol A (the blue plot in figure 4.1), we see a continuous increase in the quadratic error, which is in accordance the the expected results.

If we compare the reconstructions to the original phantom (the red plot) we see a baseline increase in the error. This is due to the inevitable artifacts which arise in the reconstruction process. This can be confirmed with the red plot for protocol A, which is the difference in the full-scale reconstruction of the phantom compared to the phantom itself. Notably, if we compare the quadratic error for the reconstructions of the different protocols to the original phantom, we see that protocol E has a lower error than both protocols C_1 and D.

The lower error of protocol E can be explained with the difference in the total amount of recorded projections. For protocol D we simulated a total amount of 4502 projections

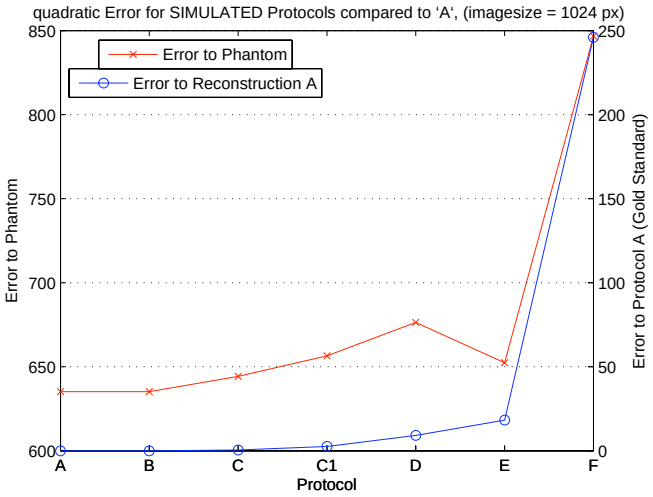

Figure 4.1.: Quadratic error of the difference image between the reconstruction of the different protocols and the gold standard. The blue plot (∘) shows the quadratic error between the protocol and the reconstruction of the gold standard, the red plot (×) shows the quadratic error between the protocol and the phantom without reconstruction.

while for protocol E we obtain 500 projections more.

The lower error for E compared to C_1 can only be explained with the bigger difference between the center and the ring scan for these protocols which introduces interpolation errors when the simulated projections are concatenated into one projection image prior to reconstruction.

CHAPTER 5

Experimental proof

5.1. Materials and methods

To test our predictions obtained through the simulations of the different protocols we recorded tomographic scans of an existing glutaraldehyde-fixed lung tissue sample obtained from a Sprague-Dawley rat 60 days after birth. The details of the animals and sample preparation have been described by Tschanz et al. [27] and Tsuda et al. [18], respectively. We used this sample for tomographic scans, since it has already been recorded at TOMCAT and we thus were able to compare the new scanning protocols to prior tomographic data-sets both in detail and on a broad scale.

All the scans have been performed at a beam energy of 17.5 keV, which is advantageous both in terms of absorption in the sample and detector efficiency. The scan has been performed with an adaptation of a present scanning script for the interaction with the EPIC-System (Experimental Physics and Industrial Control System, `http://www.aps.anl.gov/epics/`), which is controlling the beamline. The sample in the sample holder was not touched in-between the different scans. All the parameters like filename, sample-position in relation to the beam, rotation angles and amount of projections to obtain have been set beforehand in the script and the scans have been performed as a batch job without manual intervention.

5.2. Post-processing and reconstruction

Since we wanted to not only work with one slice of the different protocols, we developed a MATLAB-script (see appendix A.3) to read the different projection images from disk, to concatenate these images into one projection, to perform the sinogram generation and reconstruct full slices of the sample with a big field of view. Since at TOMCAT there are highly optimized C++-routines present to for these tasks, we used MATLAB only for reading and concatenating the projections into one big projection (1024×3072 pixels) and for the output of the correct command-line parameters for the necessary routines to generate the sinograms and reconstruct the slices.

After reconstructing 8 slices for each protocol we plotted the quadratic error of the difference image between the protocols and the gold standard to have a comparison of the experiments with the simulation.

5.3. Results

We were able to obtain wide field scans of our sample with a combined FOV three times the size of the camera window. This has been made possible by a thorough calibration of the distances visible in the preview window prior to the start of the batch job. After we recorded 13 different scan-jobs (3 jobs for protocol A and 2 jobs for every other protocol) in 3 hours and 18 minutes, the reconstructions of each sample have been performed using MATLAB to set the correct parameters for the command line programs `prj2sin` and `sin2rec`. These parameters varied from protocol to protocol.

A detail of one slice for each protocol is shown in figure 5.1. We immediately see that the seam line between the central scan and the ring scan is visible, which is undesired. A solution to this problem is presented in section 5.5.

In figure 5.2 we plotted the averaged error over 8 reconstructed slices of each protocol. The error bars for each protocol show the standard deviation of the error of the single slices.

We see that the error increases for decreasing projection numbers. In contrary to the simulation the error does not increase continuously for all protocols except E, but decreases from B to E and increases again for protocol F. A possible explanation for this fact is discussed in section 5.4.

5.4. Discussion

The results from the experimental proof of the simulation show the same trend as in the simulation. We again see – as expected – an increase of the quadratic error compared to protocol A. The quadratic error does though not increase continuously for all the protocols except E, but decreases from B to E and increases again for F.

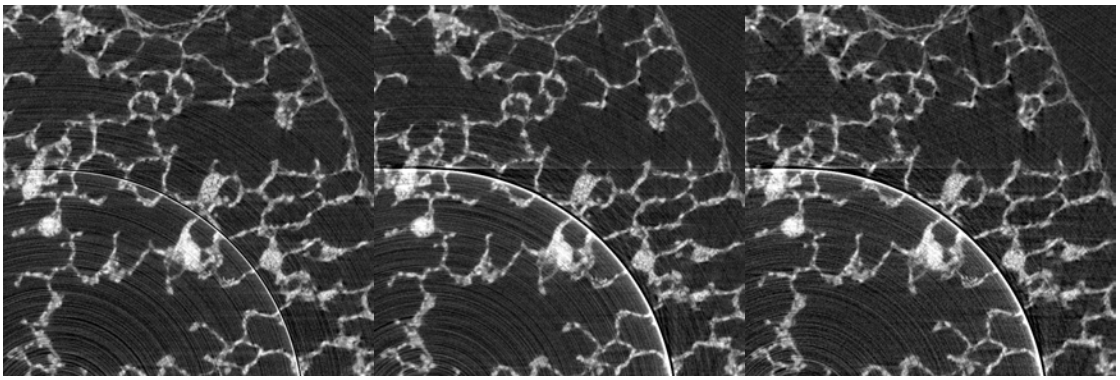

(a) Protocol A, Slice 512 **(b)** Protocol B, Slice 512 **(c)** Protocol C, Slice 512

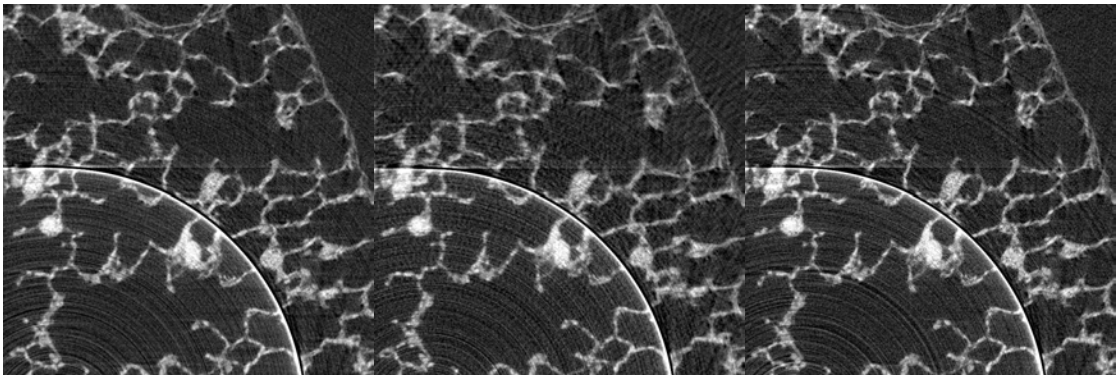

(d) Protocol D, Slice 512 **(e)** Protocol E, Slice 512 **(f)** Protocol F, Slice 512

Figure 5.1.: Detail of the concatenated Images for the different protocols. The original images are 3072×3072 pixels in size, the images shown here are detailed outtakes with a size of 764×764 pixels. Note the visible seam line as a bright quarter circle in the lower left of all the images. This is discussed in section 5.4

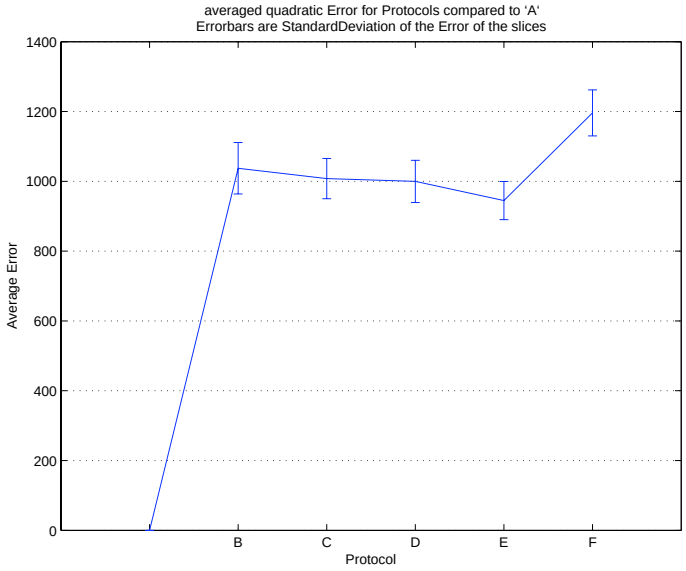

Figure 5.2.: Averaged quadratic error for the different protocols compared to the gold standard, which is protocol A (name not shown, value shown as zero). The error bars show the standard deviation of the quadratic error for the 8 different slices that have been calculated for each protocol.

An immediately visible problem with the slices that have been reconstructed from the concatenated projection images is the visible seam line at the joint between the center and the ring scan. This is due to the slight variation in the rotation axis, which we have not accounted for in the setup of the scans. We have calibrated the distances of the camera window compared to the movement of the sample stage. Our calculations showed that while moving the sample one length of FOV to the side, we did not control for the shift in the rotation axis. Since the rotation axis of the sample has not been perfectly aligned in the middle of the camera window, we were not able to correctly concatenate the three single projection images to a single big one. We calculated that for the first projections we have been missing approximately four pixels at the junction line, while having four pixels too much at the position 180° away of it.

A consequence of this is also, that at a rotation of 180° from the start of the scan the images overlapped for approximately two pixels per image. The result of this can be seen in figure 5.1, where the reconstructed slices show a distinct bright arch at the seam line between the concatenated projections. This bright arch contributes differently to the total amount of the error for each protocol, since the difference image used for the calculation of this error varies greatly, resulting in a big influence on the average error calculated in figure 5.2.

5.5. Overlapping scans

We have mentioned before that at TOMCAT there is the possibility to record a so-called stacked tomogram, where single scans are stacked vertically on top of each other. This is possible due to the high positioning precision of the total end-station and some simple calibration measures prior to scanning a vertically. The assumption that a laterally stacked scan is also possible with minute calibration led to the problems with the missing pixels at the junction line between the center and the ring, as mentioned above.

We have thus started to develop a method where we obtain slightly overlapping scans which enables a correct stitching and concatenation of the sub-scans. An overlapping scan avoids the need for calibration while slightly diminishing the available FOV. We show later on, that an overlap of 15 percent between the transmission images from each sub-scan is suitable for the correct stitching of the lateral scans into one projection image.

At first we tried to obtain a correct cutline between the overlapping regions using the cross-correlation between these image segments. The cutline defines the position at which one image has to be cropped to obtain a correct match between the adjacent images. Since the adjacent images do slightly overlap, we make it unnecessary to correct for the slight variation in the rotation axis of the sample and can just crop the images to the correct horizontal size at the cutline. Using a fourier transformation in a MATLAB script (see appendix A.4) we plotted the cross-correlation between the overlapping parts. Using the minima of this plot for the calculation of the cutline we were able to stitch the images correctly into one big projection. Unfortunately we have seen that the resulting cutline between the overlapping segments is not very robust in terms of position, especially in highly uniform samples like lung tissue with its spongy structure inherently is. We had to use the cross-correlation between multiple horizontal lines for up to about a third of all the lines of the image height to achieve good results. This led to long calculation times and nevertheless did not lead to the correct cutline for all the projections, leading to wrong reconstructions. Albeit not being a very stable approach, we have shown that this approach can lead to precise reconstructions of the samples and eliminates the problem mentioned with the arching bright cutline, so using slightly overlapping scans is a viable method to obtain scans with FOV much bigger than the camera windows width.

Just recently, we have been developing a more stable method for the calculation of the position of the cutline between the overlapping scans using the mutual difference in the overlapping parts of the images. We are using the minimum of the difference function of the overlapping segments to obtain the position of the cutline. This enables us to calculate the cutline from as few as three horizontal lines of the projection images with very high reproducibility.

This concatenating approach will be developed in the near future and deployed as a simple to use tool at the beamline, for now the concatenation of the single overlapping projection images into one big projection has to be performed semi-manually using a

MATLAB script implementing the method mentioned above.

To proof this method, we recorded two samples with slightly overlapping sub-scans and were able to achieve reconstructions of the samples with a side length of 8192 pixels. The reconstruction of one of these scans is shown in figure 5.3. A side length of 8192 corresponds to an achieved FOV of 5.734 mm if we keep in mind that at a 10× magnification the pixel size is approximately 0.70 µm. We scanned a known sample of a Sprague-Dawley rat 4 days after birth at a beam energy of 12.6 keV. The sample is a part of the right lower lung lobe embedded in paraffin and was scanned with five scans overlapping each other by 15 percent. The scanning protocol was defined using the MATLAB script described in section 5.6 and scanned with the python script mentioned in the same section.

We have chosen an intermediate quality of the protocol as it was intended as a proof of concept and we did not aim for maximal quality in the reconstruction. In total we obtained 25896 projections of the sample during one hour and 44 minutes, measured from the start of the python script until the last image of the fifth sub-scan was written to the disk. The projection from each sub-scan have been concatenated into one big projection using a MATLAB script, sinograms of these concatenated projections were produced using `prj2sin` and some slices were reconstructed using `gridrec`, since the filtered backprojection program currently present at the beamline only works for slices with a side length smaller than 8096 pixels.

In figure 5.3 (a) we see a merged projection image, acquired from five sub-scans. The flat-field correction of the different sub-scans is still not perfect, further investigations will be necessary to perfectly merge different sub-scans into one big projection image without varying brightness. Currently a summer student at TOMCAT is developing a flat field tracking system which should increase the quality of the flat field correction. Figure 5.3 (b) shows one reconstructed slice of the right under lung lobe of a rat with a maximum tissue diameter of 5250 pixels corresponding to approximately 3.7 mm scanned at a resolution of 0.7 µm per pixel. In figure (b) we see some radial artifacts in the outer parts of the sample, which arise through the sub-optimal concatenation of the images, since we are still developing a stable method with sub-pixel precision.

5.6. Integration of the wide field scan at the beamline

To allow the user to choose not only different protocols, but also to have a mean of choosing a sensible one for his needs, we developed a combination of two scripts to perform the scan (see appendices A.5 and A.6). The first script asks the user for the details on his scan and outputs a graph with different proposed protocols. The user inputs the diameter of the sample, the desired overlap between the single scans, samplename and details on the optical setup like magnification, binning and calibration if desired.

On the basis of the protocols proposed in chapter 3 we then calculate different protocols

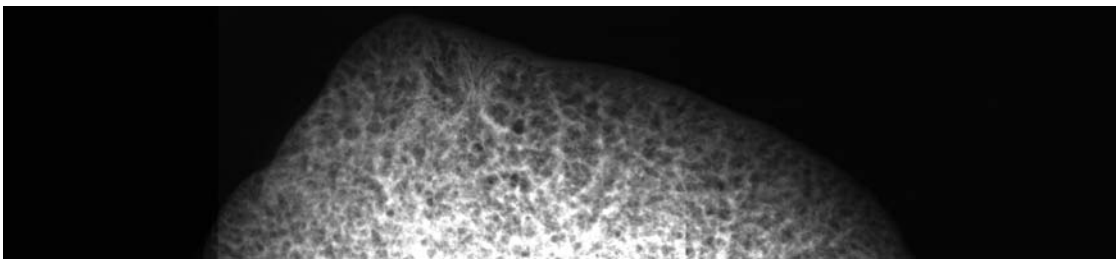

(a) Concatenated projection image with a size of 4502×1024 pixels size. Note the slightly varying brightness between the sub-scans.

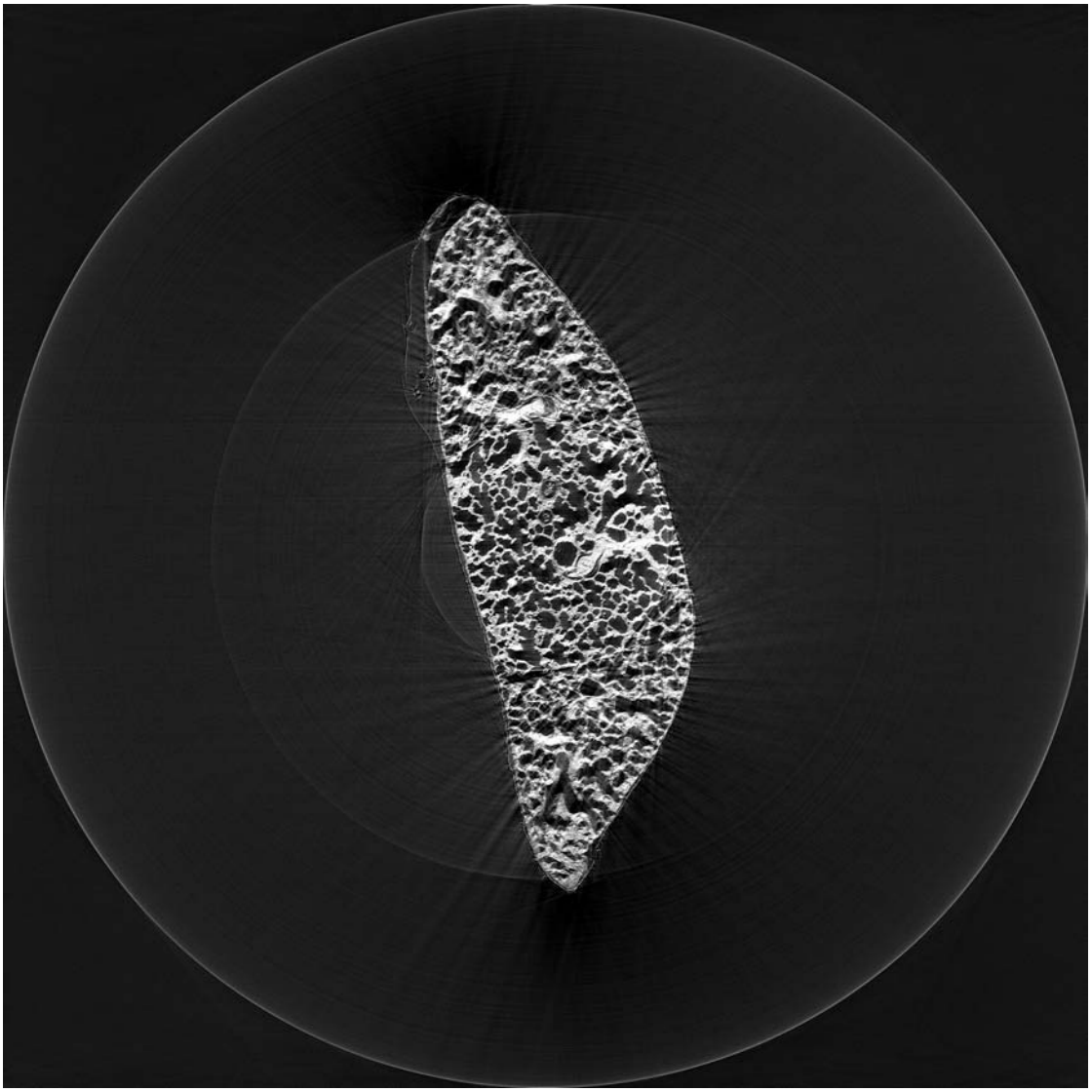

(b) Reconstructed slice of scanned lung tissue with a size of 8192×8192 pixels size. The image has been resized to 2048×2048 pixels and the gray values have been normalized for display purposes. The seam line where the sub-scans have been joined is visible, especially in the left part of the image

Figure 5.3.: Images resulting from a wide field scan with five overlapping sub-scans

and plot the expected quality versus the time expected for the scan, as can be seen in figure 5.4. After the user has chosen a suitable scanning protocol matching the expected quality standard, MATLAB writes a preference file on the disk which is subsequently parsed by the second script which then starts each sub-scan at the beamline through direct interaction with the EPIC system.

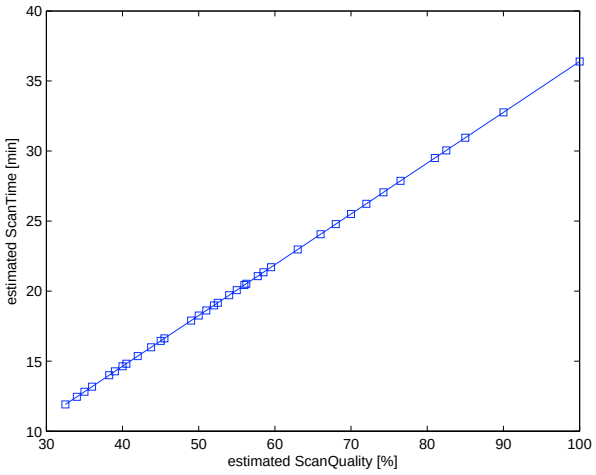

Figure 5.4.: Plot of expected quality versus estimated time needed to scan the sample. The user at the beamline is then free to choose whatever protocol fits his needs, selects a point on the line (the boxes show the different protocols) and MATLAB chooses the protocol which corresponds to the point chosen by the user. The parameters of the whole scan are subsequently written to a text file. This text file contains for each sub-scan the number of projections, the so-called inbeam position corresponding to the position of the sample laterally to the beam center and the start- and stop-angles of the rotation and is parsed by a script that interacts with the beamline control system without any user interaction.

CHAPTER 6

Concluding remarks and outlook

We have developed a method to record tomographic images with a FOV that is bigger than the now available FOV at TOMCAT. We developed different protocols to be able to simulate different scanning qualities in chapter 4 and proved the simulated protocols experimentally in chapter 5. In addition to this, we developed a preliminary mean for the users to perform a quality guided wide field scan using a combination of a MATLAB and a Python script. The user at the beamline is free to choose a scan that fits his or her needs, be it either a very fast wide field scan to obtain a quick overview over the full sample or an accurate wide field scan to record a tomographic scan of the sample with maximal quality.

We have seen that while we have been recording precise scans after a thorough calibration of the beamline we were not able to simply concatenate the projection images of the sub-scans into one big scan like we presumed it would be possible, but need to record the sub-scans in such a manner that the border regions of the scans overlap by a small percentage. This enables us to extract a correct cutting line between the sub-scans and thus avoids the problem with the alignment of the rotation axis.

We tried different ways of extracting the correct cutting line, first using the cross correlation and then a method using the difference in the overlapping image parts. In the end, a correct algorithm to join the overlapping sub-scans into one big scan prior to the reconstruction has been found and described in section 5.5.

We were able to perform a scan with a FOV nearly five times the camera window size, minus an overlap of 15 percent. A reconstruction of multiple slices of this scan proves that the method is applicable in general. The full integration into the workflow of the beamline has not been achieved during the term of this master thesis. First steps to

this have been achieved with a script that asks the user about the details of the scan and writes a preference file to the disk, which can then be parsed by a second script that is able to perform the desired sub-scans in an unattended way. The post processing steps necessary needed to reconstruct the sample are still quite a bit of manual work but will gradually migrate to an automated way. The final integration at the beamline for the end-user will probably be achieved by either the beamline staff or an upcoming internship student, which can continue on the paths this work has laid.

6.1. 360° versus 180° scans

In the course of the discussion of the results with my supervisor, we decided that the sub-scans should all be performed at $i \times 180°$ and not at $i - 1 \times 360°$ plus one central scan at 180° (where i is an odd number). This is in accordance with the facts mentioned above, where we have shown that it is vital that we have a mean of correcting for not perfectly aligned rotation axes. Albeit we introduce more scanning overhead through acquisition of additional dark and flat images and through more movement steps of the sample, we gain a much simpler method of stitching the images and we do not have to control as carefully for the rotation axis. The wide field scanning protocol will be implemented at the beamline using overlapping 180° scans.

6.2. Partial reconstructions of the scanned samples

One of the reasons to record a wide field scan is the possibility of extracting arbitrary details of the sample without performing a new scan using a reconstruction based on a ROI anywhere in the sample. Since we already scanned the samples with optimal resolution, we are able to reconstruct partial sinograms using only parts of the sub-scan transmission images and reconstruct a ROI from the original sample with virtually unlimited resolution.

Bibliography

[1] M. Stampanoni, A. Groso, A. Isenegger, G. Mikuljan, Q. Chen, D. Meister, M. Lange, R. Betemps, S. Henein, and R. Abela. TOMCAT: A beamline for TOmographic Microscopy and Coherent rAdiology experimenTs. *AIP Conference Proceedings*, 879(1):848–851, 2007. doi: 10.1063/1.2436193. URL `http://link.aip.org/link/?APC/879/848/1`. 1.1, 1.4

[2] A.J. Davenport, C. Padovani, B.J. Connolly, N.P.C. Stevens, T.A.W. Beale, A. Groso, and M. Stampanoni. Synchrotron X-Ray Microtomography Study of the Role of Y in Corrosion of Magnesium Alloy WE43. *Electrochemical and Solid-State Letters*, 10:C5, 2007. 1.1

[3] A. Carminati, A. Kaestner, H. Flühler, P. Lehmann, D. Or, E. Lehmann, and M. Stampanoni. Hydraulic contacts controlling water flow across porous grains. *Physical Review E*, 76(2):26311, 2007. 1.1

[4] E. Gallucci, K. Scrivener, A. Groso, M. Stampanoni, and G. Margaritondo. 3D experimental investigation of the microstructure of cement pastes using synchrotron X-ray microtomography (μCT). *Cement and Concrete Research*, 37(3):360–368, 2007. 1.1

[5] M. M. Miedaner, T. Huthwelker, F. Enzmann, M. Kersten, M. Stampanoni, and M. Ammann. X-ray tomographic characterization of impurities in polycrystalline ice. *Physics and Chemistry of Ice: proceedings of the 11th International Conference on the Physics and Chemistry of Ice held at Bremerhaven, Germany on 23-28 July, 2006*, pages 399–+, 2007. 1.1

[6] P. Trtik, J. Dual, D. Keunecke, D. Mannes, P. Niemz, P. Stähli, A. Kaestner, A. Groso, and M. Stampanoni. 3D imaging of microstructure of spruce wood. *Journal of Structural Biology*, 159(1):46–55, 2007. 1.1

[7] S. Vaucher, P. Unifantowicz, C. Ricard, L. Dubois, M. Kuball, J.M. Catala-Civera, D. Bernard, M. Stampanoni, and R. Nicula. On-line tools for microscopic and macroscopic monitoring of microwave processing. *Physica B: Physics of Condensed Matter*, 398(2):191–195, 2007. 1.1

[8] S. Heinzer, R. Müller, M. Stampanoni, R. Abela, E. P. Meyer, A. Ulmann-Schuler, and T. Krucker. Computer-based analysis of microvascular alterations in a mouse model for Alzheimer's disease. In *Medical Imaging 2007: Physiology, Function, and Structure from Medical Images. Edited by Manduca, Armando; Hu, Xiaoping P.. Proceedings of the SPIE, Volume 6511, pp. 651104 (2007).*, volume 6511 of *Presented at the Society of Photo-Optical Instrumentation Engineers (SPIE) Conference*, March 2007. doi: 10.1117/12.708869. 1.1

[9] S. Heinzer, G. Kuhn, T. Krucker, E. Meyer, A. Ulmann-Schuler, M. Stampanoni, M. Gassmann, H.H. Marti, R. Müller, and J. Vogel. Novel three-dimensional analysis tool for vascular trees indicates complete micro-networks, not single capillaries, as the angiogenic endpoint in mice overexpressing human VEGF165 in the brain. *Neuroimage*, 39(4):1549–1558, 2008. 1.1

[10] C. Hintermüller, J. S. Coats, A. Obenaus, G. Nelson, T. Krucker, and M. Stampanoni. Assessment of radiation induced alterations in brain micro vasculature using x-ray tomographic microscopy. Poster - 18th Annual NASA Space Radiation Investigators' Workshop, June 2007. 1.1

[11] Johannes C. Schittny, Sonja I. Mund, and Marco Stampanoni. Evidence and structural mechanism for late lung alveolarization. *Am J Physiol Lung Cell Mol Physiol*, 294(2):L246–254, 2008. doi: 10.1152/ajplung.00296.2007. URL `http://ajplung.physiology.org/cgi/content/abstract/294/2/L246`. 1.1

[12] R. Voide, G.H. van Lenthe, M. Stauber, P. Schneider, P.J. Thurner, P. Wyss, M. Stampanoni, and R. Müller. Functional microimaging: a hierarchical investigation of bone failure behavior. *J. Jpn. Soc. Bone Morphom.*, 18:9–21, 2008. 1.1

[13] Philipp Schneider, Martin Stauber, Romain Voide, Marco Stampanoni, Leah Rae Donahue, and Ralph Mller. Ultrastructural properties in cortical bone vary greatly in two inbred strains of mice as assessed by synchrotron light based micro- and nano-ct. *Journal of Bone and Mineral Research*, 22(10):1557–1570, 2007. doi: 10.1359/jbmr.070703. URL `http://www.jbmronline.org/doi/abs/10.1359/jbmr.070703`. 1.1

[14] N.J. Gostling, C.W. Thomas, J.M. Greenwood, X. Dong, S. Bengtson, E.C. Raff, R.A. Raff, B.M. Degnan, M. Stampanoni, and P.C.J. Donoghue. Deciphering the fossil record of early bilaterian embryonic development in light of experimental taphonomy. *Evolution & Development*, 10(3):339–349, 2008. 1.1

[15] E.M. Friis, P.R. Crane, K.R. Pedersen, S. Bengtson, PC Donoghue, G.W. Grimm, and M. Stampanoni. Phase-contrast X-ray microtomography links Cretaceous seeds with Gnetales and Bennettitales. *NATURE-LONDON-*, 450(7169):549, 2007.

[16] J.W. Hagadorn, S. Xiao, P.C.J. Donoghue, S. Bengtson, N.J. Gostling, M. Pawlowska, E.C. Raff, R.A. Raff, F.R. Turner, Y. Chongyu, et al. Cellular and Subcellular Structure of Neoproterozoic Animal Embryos. *Science*, 314(5797): 291–294, 2006.

[17] P.C.J. Donoghue, S. Bengtson, X.P. Dong, N.J. Gostling, T. Huldtgren, J.A. Cunningham, C. Yin, Z. Yue, F. Peng, and M. Stampanoni. Synchrotron X-ray tomographic microscopy of fossil embryos. *Nature*, 442(7103):680–683, 2006. 1.1

[18] A. Tsuda, N. Filipovic, D. Haberthür, R. Dickie, Y. Matsui, M. Stampanoni, and J. C. Schittny. Finite element 3D reconstruction of the pulmonary acinus imaged by synchrotron X-ray tomography. *J Appl Physiol*, 105(3):964–976, 2008. doi: 10.1152/japplphysiol.90546.2008. URL `http://jap.physiology.org/cgi/content/abstract/105/3/964`. 1.1, 5.1

[19] SLS Web Site - Description. Website, 04 2008. URL `http://tinyurl.com/5kdsux`. 1.3

[20] M. Stampanoni, A. Groso, A. Isenegger, G. Mikuljan, Q. Chen, A. Bertrand, S. Henein, R. Betemps, U. Frommherz, P. Böhler, D. Meister, M. Lange, and R. Abela. Trends in synchrotron-based tomographic imaging: the SLS experience. In *Society of Photo-Optical Instrumentation Engineers (SPIE) Conference Series*, volume 6318 of *Society of Photo-Optical Instrumentation Engineers (SPIE) Conference Series*, Aug. 2006. doi: 10.1117/12.679497. URL `http://link.aip.org/link/?PSI/6318/63180M/1`. 1.4

[21] Wikipedia. Szintillator — wikipedia, die freie enzyklopdie, 2009. URL `http://is.gd/1KgaS`. [Online; 25. August 2008]. 1.4.1

[22] B. A. Dowd, G. H. Campbell, R. B. Marr, V. V. Nagarkar, S. V. Tipnis, L. Axe, and D. P. Siddons. Developments in synchrotron x-ray computed microtomography at the National Synchrotron Light Source. *SPIE Developments in X-Ray Tomography II, Denver, CO (US), 07/18/1999–07/23/1999*, 3772:224–236, September 1999. 2

[23] Avinash C. Kak, Author, Malcolm Slaney, Author, Ge Wang, and Reviewer. Principles of computerized tomographic imaging. *Medical Physics*, 29(1):107–107, 2002. doi: 10.1118/1.1455742. URL `http://www.slaney.org/pct/`. 2, 3.1

[24] Johann Radon. Über die Bestimmung von Funktionen durch ihre Integralwerte längs gewisser Mannigfaltigkeiten. *Berichte Sächsische Akademie der Wissenschaften*, 69: 262–277, 1917. 1

[25] LA Shepp and BF Logan. The Fourier reconstruction of a head section. *IEEE Trans. Nucl. Sci*, 21(1):21–43, 1974. 2

[26] Christoph Hintermüller, Federica Marone, Andreas Isenegger, and Marco Stampanoni. Image processing pipeline for fast Synchrotron based X-Ray Micro-Tomographic Microscopy. *Journal of Synchrotron Radiation*, 2009. submitted. 3.2

[27] Stefan A Tschanz, Andrew N Makanya, Beat Haenni, and Peter H Burri. Effects of neonatal high-dose short-term glucocorticoid treatment on the lung: a morphologic and morphometric study in the rat. *Pediatr Res*, 53(1):72–80, Jan 2003. 5.1

APPENDIX A

Scripts used in this master thesis

A.1. MATLAB- simulation.m and accompanying functions

A.1.1. simulation.m

The script `simulation.m` uses the functions `h_slabinterpolate.m` and `h_PadImage.m` to perform sub-tasks. Both those files are listed in the subsections below this one[1].

A.1.2. h_slabinterpolate.m

A.1.3. h_PadImage.m

A.2. MATLAB - do_simulate.m

A.3. MATLAB - do_CompareReconstructions.m

The function `do_CompareReconstructions.m` uses the function `readDumpImage.m` written by Stefan Heinzer, IBT ETH/Uni Zürich. This function is used to read the raw data files of TOMCAT from disk. Since I cannot publish this function, the present MATLAB script has to be adapted to read .tif-files for every instance of `readDumpImage.m`.

[1] I've removed all the MATLAB and Python-code, since the whole master thesis is currently written into a manuscript for the Journal of Synchrotron Radiation...

A.4. MATLAB - do_correlationFFT.m

A.5. MATLAB - widefieldscan.m and accompanying function

A.5.1. widefieldscan.m

The script `widefieldscan.m` uses the functions `h_reducesegments.m` for the calculation of the iterative reduction of the number of projections in the central and outer parts of the scan. This file is listed in the subsection below.

A.5.2. h_reducesegments.m

A.6. Python - widefieldscan.py